ACS Catalysis

Research Article

pubs.acs.org/acscatalysis

Insights into the Surface-Defect Dependence of Photoreactivity over CeO_2 Nanocrystals with Well-Defined Crystal Facets

Dong Jiang,[†,‡] Wenzhong Wang,[*,†] Ling Zhang,[†] Yali Zheng,[†,‡] and Zhong Wang[†,‡]

[†]State Key Laboratory of High Performance Ceramics and Superfine Microstructure, Shanghai Institute of Ceramics, Chinese Academy of Sciences, 1295 Dingxi Road, Shanghai 200050, P.R. China

[‡]University of Chinese Academy of Sciences, Beijing 100049, P.R. China

Supporting Information

ABSTRACT: Crystal facet engineering (CFE) has been widely employed to regulate the photoreactivity of crystalline materials, mostly concerning the surface atomic and electronic structures. However, surface defects ubiquitous in real catalysts have long been less recognized. An integrated examination of various influence factors is necessary for the elucidation of an accurate structure−function relationship. Herein, we carefully studied the heterogeneous photoreactivity of CeO_2 nanocrystals (NCs) with well-defined crystal facets in multiple processes, including photocatalytic oxidation of volatile organic compounds (VOCs), O_2 evolution, and ·OH generation. Variable reactivity priorities were found between different nanoshapes as well as samples of identical nanoshapes. With integrated examinations of the coexisting surface factors (i.e., atomic, electronic, and defect structures), surface defects were evidently proved to compete with other surface factors in deciding the final photoreactivity orders. Surface-defect structure (e.g., Ce^{3+} ions and O vacancies) was suggested to greatly influence the surface properties of ceria NCs, including the activation of reactants as well as the mobility of surface lattice oxygen. The results clearly confirm the surface-defect dependence of photoreactivity and provide further insights into the complex surface effects in semiconductor photocatalysis. It also underscores the significance of surface-defect structure as an essential supplement to the traditional CFE strategy for achieving desired solar energy utilization.

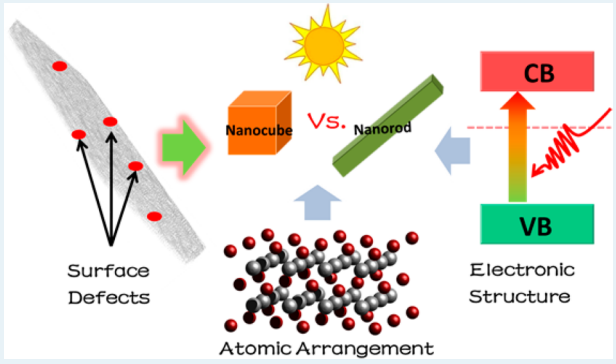

KEYWORDS: *photocatalysis, water splitting, VOCs, oxygen vacancies, hydroxyl radicals*

INTRODUCTION

As one commonly employed approach to optimizing the reactivity and selectivity of crystalline materials, crystal facet engineering (CFE) has initiated a flourishing interest in semiconductor photocatalysis.[1−4] Essentially, the basis of this strategy is the consensus that the heterogeneous catalytic performance of nanocrystals (NCs) is dominated by the anisotropic surface chemistry. As such, crystal facets with a higher percentage of under-coordinated atoms as active sites have long been pursued, such as the {001} facets of anatase TiO_2.[1,5,6] However, photocatalysis is the integration of photoexcitation, which involves light harvesting as well as charge carriers output, and surface catalysis, which includes the utilization of photoinduced e^-/h^+ pairs.[7,8] In order to achieve ideal solar energy conversion, the above two sequential steps must be guaranteed concurrently.[7] Therefore, CFE, which mainly concerns surface reactions, may not always be the exclusive determinant in catalyst design. One experimental verification is that Liu et al. found an unexpected reactivity order ({001} < {101} < {010}) for anatase TiO_2 in photocatalytic ·OH generation and H_2 evolution.[2] A cooperative mechanism of surface atomic structure and surface electronic structure was further proposed to modify the pristine CFE strategy.[2,9] However, it is crucial but less recognized in CFE that surface defects ubiquitous in real catalysts play essential roles in both photoexcitation and surface catalysis, including defect-mediated light absorption, electron capture, and reactant activation.[10−12] Up to now, the discussions on photocatalysts with specific crystal facets are generally one-sided. An integrated examination of various influence factors is necessary before the conclusion of an accurate structure−function relationship.

Fluorite ceria is technologically important due to its wide applications in catalysis.[13−16] Besides, it has been studied as a promoter in photocatalytic pollutant degradation, water oxidation, and selective organics transformation.[7,17,18] Recently, we proved within CeO_2 that the coupled electronic and ionic conduction can help integrate low temperature catalysis into photocatalysis, inducing greatly enhanced activity as well as improved resistance to deactivation.[19,20] In catalysis, the past decade has seen systematic studies on shape-controlled CeO_2 with well-defined surface planes, including CO oxidation,

Received: June 1, 2015
Revised: July 9, 2015
Published: July 10, 2015

DOI: 10.1021/acscatal.5b01128
ACS Catal. 2015, 5, 4851−4858

oxygen storage, and water−gas-shift (WGS).[14,21−23] Actually, since the 1990s and even before, theoretical simulations have tried to probe the heterogeneous reactivity of different CeO_2 crystal facets, indicating dipolar {100} with the highest surface energy, followed by {110}, and then the most stable {111}.[24−28] However, experimental results in some reports showed evident divergence with the suggested reactivity order.[29−32] For instance, CeO_2 nanorods ({110} + {100}) were more reactive than {100}-dominated nanocubes for CO oxidation.[29,30] In-depth studies by Nolan et al. revealed that the {110} facet has the lowest vacancy formation energy, different with the stability order as evaluated by surface energy.[26,27] Moreover, CeO_2-based catalysis in various processes may also be controlled by the nature of defect sites, including CO oxidation and WGS.[14,33,34] Li et al. found that oxygen vacancy clusters can greatly promote the reducibility of ceria nanorods, rendering the most stable {111} facet with superior activity in CO oxidation, compared to the {110} facet embedded with isolated vacancy associates.

To our knowledge, no CFE studies on CeO_2-based photocatalysis have been conducted. Given the thorough knowledge of defect-mediated surface chemistry in CeO_2, a systematic exploration on multiple photocatalytic processes over CeO_2 with well-defined crystal facets can be expected. In this study, we elaborately discussed the heterogeneous reactivity of regularly shaped CeO_2 NCs with different surface planes in multiple photocatalytic processes, including the oxidation of VOCs, O_2 evolution, and ·OH generation. Surface-defect structure (e.g., Ce^{3+} ions and O vacancies) was clearly suggested to influence the surface properties of ceria NCs, including the reactants activation as well as the mobility of surface lattice oxygen. In addition to the surface atomic and electronic structures, the results evidently proved the surface-defect dependence of photoreactivity. That is, there existed a competition among the coexisted surface factors (i.e., atomic, electronic, and defect structures) in deciding the final photocatalytic performance.

EXPERIMENTAL SECTION

Material Synthesis. The synthesis of the two ceria nanoshapes has been described in previous reports.[14,22] Briefly, CeO_2 nanocubes (C) and nanorods (R) were prepared by a hydrothermal process at different hydrothermal temperatures. For C−Cl and R−Cl, $CeCl_3{\cdot}7H_2O$ (2 mmol) was added into the NaOH aqueous solution (6 M, 40 mL) and transferred to the 50 mL Teflon lined stainless steel autoclaves, and then heated at 180 and 110 °C for 24 h, respectively. For R−NO, the preparation conditions were identical with that of R−Cl, except that Ce $(NO_3)_3{\cdot}6H_2O$ was used as the cerium precursor. After the hydrothermal treatment, the precipitates obtained were washed with deionized water and anhydrous ethanol for several times, followed by freeze-drying and drying at 60 °C in air overnight, successively. Finally, the powders were calcined at 400 °C in air for 3 h before further characterizations and photocatalytic reactions.

Material Characterization. The powder X-ray diffraction (XRD) patterns were recorded on a Rigaku D/MAX 2250 V diffractometer using monochromatic Cu Kα radiation, with an operating voltage of 30 kV and current of 100 mA. The morphologies and microstructures of as-prepared samples were investigated by transmission electron microscopy (TEM) and selected area electron diffraction (SAED) with a TecnaiG2 F20 S-Twin. Diffuse reflectance spectra were obtained on a UV−vis spectrophotometer (Hitachi U-3010) using $BaSO_4$ as the reference. The N_2-sorption measurements were performed at 77 K using a Micromeritics Tristar 3000 analyzer. X-ray photoelectron spectroscopy (XPS) analysis was performed on ESCALAB 250 (Thermo Scientific Ltd.). The C 1s was used to correct the charge effects. Room-temperature photoluminescence (PL) was recorded on a Hitachi F-4600 fluorescence spectrophotometer. The hydrogen temperature-programmed reduction (H_2-TPR) and oxygen temperature-programmed desorption (O_2-TPD) were performed (50 mg for each sample) on a Micromeritics Chemisorb 2750, equipped with a thermal conductivity detector. Briefly, H_2-TPR was operated under a 10% H_2/Ar flow at a heating rate of 10 °C min^{-1}. For O_2-TPD, the adsorption of O_2 was performed in a 4% O_2 /He gas flow for 1 h at room temperature. Afterward, the sample was heated to 850 °C at a heating rate of 10 °C min^{-1} in a pure He gas flow. Prior to both the H_2-TPR and O_2-TPD tests, the catalyst powders were preheated under a He gas flow at 300 °C for 1 h in a quartz reactor so as to dislodge the absorbed H_2O and other organic adsorbates, and then cooled to room temperature.

Photocatalytic Tests. Various photocatalytic tests were performed under the irradiation of a Xe lamp (500 mW cm^{-2}) at room temperature (25 °C), including the degradation of volatile organic compounds (VOCs), O_2 evolution, and ·OH generation. In each test without special statement, 50 mg of catalyst powder was used for each CeO_2 sample. The dosage (50 mg) here was determined according to the high-loft feature of as-prepared catalyst powders (Figure S1). With this dosage, the powder dispersions of three CeO_2 NCs are sufficiently concentrated to absorb the incident photons to a similar extent. *(1) VOCs degradation.* Photocatalytic oxidation of propane (25 ppm) and propylene (25 ppm) was operated in a gas-closed vitreous reactor (650 mL) with a quartz window on the top and a double-walled jacket. During the tests, catalyst powders were spread at the bottom of the reactor. The VOCs oxidation was monitored by the decrease of C_3H_6 and C_3H_8, by GC analysis (GC 7900, Techcomp) with a TM plot-Al_2O_3/S capillary column and a flame ionization detector (FID). *(2) Water splitting.* O_2 evolution by water splitting was conducted in a Pyrex cell (600 mL) with a quartz window on top, in the presence of $AgNO_3$ (0.01M, 200 mL) as an electron quencher. The amount of evolved O_2 was determined by using online gas chromatography (GC 7890 II, Techcomp) with a thermal conductivity detector (TCD) (NaX zeolite column, N_2 carrier). Prior to irradiation, N_2 was purged through the cell to remove residual oxygen in water. *(3) •OH generation.* The formation of hydroxyl radicals on the surface of various CeO_2 samples under Xe lamp irradiation was monitored by photoluminescence (PL) in the presence of terephthalate acid (TPA) as a probe. Briefly, catalyst powder (30 mg) was added into deionized water (100 mL) containing NaOH (0.01 M) and TPA (3 mM). Before exposure to light, the suspension was stirred in the dark for 30 min. At given time intervals after irradiation, 3 mL of the suspensions was sampled and centrifuged for fluorescence analysis with a spectrophotometer (Hitachi F-4600). The formed 2-hydroxyterephthalic acid has a fluorescence signal around 425 nm by excitation of 315 nm.

Electrochemical Analysis. The electrochemical analysis was performed on a CHI 660D electrochemical workstation (Shanghai Chenhua, China) using a standard three-electrode quartz cell. A Xe lamp (CHF-XM500) was used as light source. To make a working electrode, CeO_2 powders were deposited

DOI: 10.1021/acscatal.5b01128
ACS Catal. 2015, 5, 4851−4858

Table 1. Exposed Crystal Planes, Shapes, Sizes, and BET Surface Areas of As-Prepared CeO_2

items	C−Cl	R−Cl	R−NO
shapes	cube	rod	rod
planes	{100}	{110} + {100}	{110} + {100}
sizes (nm)	30−50	(8−12)* (120−180)	(8−12)* (120−180)
BET (m^2 g^{-1})	32.7	60.2	78.5

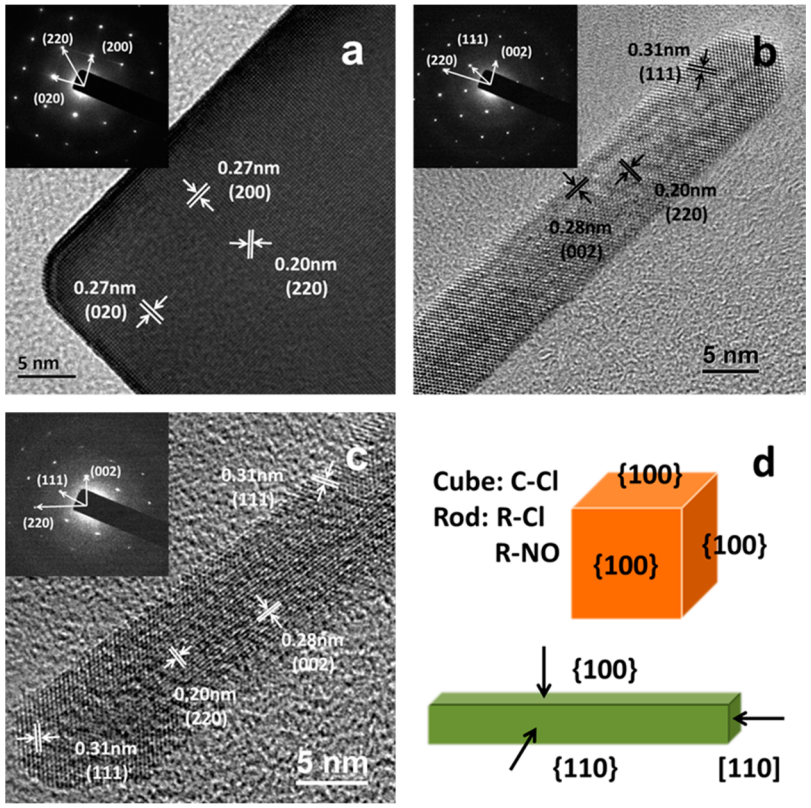

Figure 1. High-resolution transmission electron microscopy (TEM) images of C−Cl (a) view along [001], R−Cl (b) and R−NO (c) view along [1−10]. Insets are corresponding selected area electron diffraction (SAED) patterns. Geometric models of CeO_2 nanocubes and nanorods (d).

on a fluorine-doped tin oxide (FTO) substrate by nafion coating. Briefly, 10 mg of catalyst was suspended in 400 μL of 1 wt % nafion-ethanol solution and the mixtures were ultrasonically scattered for 15 min. Then, 150 μL of above slurry was coated on the FTO glass. After evaporation of ethanol, the catalyst coated FTO substrate was used as the working electrode. The flat-band potentials (V_{fb}) were estimated from Mott−Schottky plots by the electrochemical method, performed at a fixed frequency of 1000 Hz with 10 mV amplitude. The current−time curves were collected at 0.6 V vs SCE. During the measurements, the electrolyte was 0.1 M Na_2SO_4 solution (pH 6.8) and bubbled with nitrogen.

RESULTS AND DISCUSSION

Two CeO_2 nanoshapes (i.e., rods and cubes) were synthesized via a reported hydrothermal method, with the X-ray diffraction (XRD) patterns readily indexed to a cubic fluorite structure (Figure S2).[14,22] Besides, two CeO_2 nanorods were prepared with different cerium precursors (i.e., $CeCl_3$ and Ce $(NO_3)_3$). No morphology-inducing agent was introduced so as to avoid any unexpected interferences in deciding the photoreactivity of various ceria NCs. For simplicity, the three samples are named C−Cl, R−Cl, and R−NO according to the nanoshapes and precursors used. According to the transmission electron microscopy (TEM) images (Figure S3), the size of well-defined CeO_2 nanocubes (C−Cl) is in the range of 15−40 nm, whereas the two rod-like samples (R−Cl and R−NO) are 8−12 nm in width and 120−180 nm in length (Table 1).

As well characterized by the high-resolution electron microscopy and electron diffraction (Figure 1), the exposed crystal facets of single-crystal CeO_2 were clearly identified. It is shown that ceria nanocubes and nanorods are dominantly terminated by {100} and {110} + {100} facets, respectively, which agree well with previous reports.[14,22] Based on the geometric models in Figure 1d, the relative proportion of {110} planes can be roughly determined to be 52% in ceria nanorods, assuming the length and width to be 150 and 10 nm, respectively. Given the large aspect ratios, there should not be much difference in the relative proportion of {110} planes between the two rod-like samples, R−Cl and R−NO. Additionally, in Figure 1 and S3, all the three ceria samples have been characterized by a simple microscopic morphology, free of any kinds of pore structures except general random stacking of discrete nanoparticles. That is, when under light irradiation, the powder dispersions of three CeO_2 NCs can be illuminated by light to a similar extent without internal shading from pores.[35] Note that in Table 1, the BET surface areas of ceria nanorods are nearly twice that of nanocubes, closely

DOI: 10.1021/acscatal.5b01128
ACS Catal. 2015, 5, 4851−4858

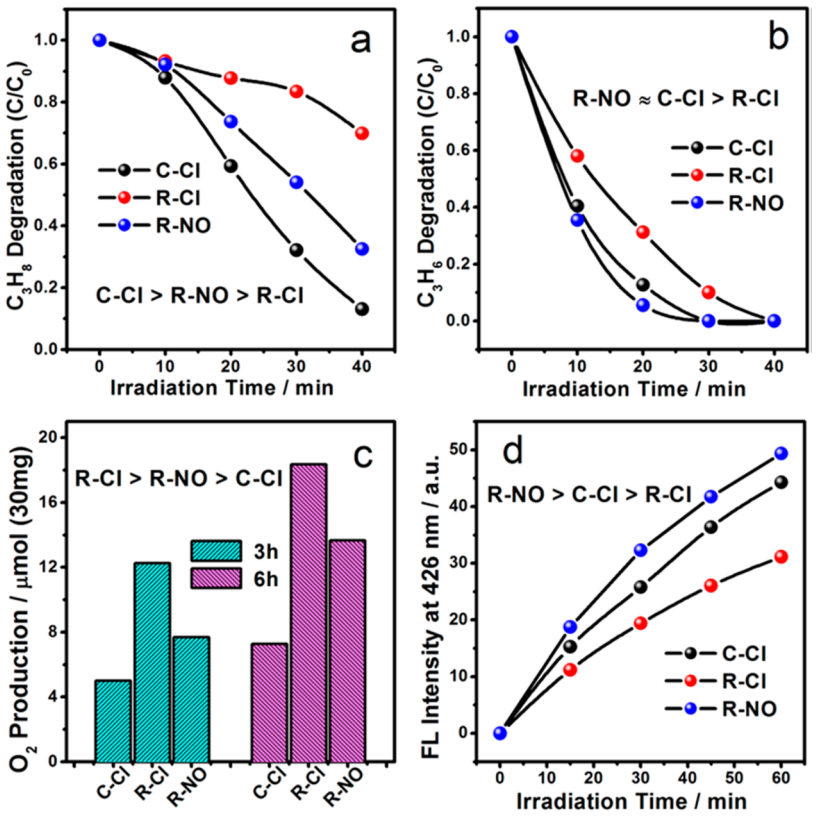

Figure 2. Photocatalytic degradation of propane (a) and propene (b). Oxygen evolution from water in the presence of $AgNO_3$ (c). Temporal evolution of fluorescence intensity at 426 nm (d). The notes inside each panel are the apparent reactivity orders before normalized by the BET surface areas.

related to their different sizes. These differences may influence the photoreactivity of different samples and should be taken into consideration to some extent.

Due to the relatively positive level position of the valence band (VB), CeO_2 has been widely studied in various photocatalytic oxidation.[7,17,18] Herein, several photo-oxidation processes were evaluated over three CeO_2 NCs (Figure 2), including the VOCs degradation, O_2 evolution as well as ·OH generation. A Xe lamp equivalent to 5 suns in illumination intensity was used to simulate the solar irradiation. Compared with our previous work, the dosage here was appropriately reduced on account of the high-loft feature of as-prepared catalyst powders (Figure S1).[36]

As shown in Figure 2a,b, within 40 min, propene (C_3H_6, 25 ppm) can be completely eliminated over all the three CeO_2 samples, whereas propane (C_3H_8, 25 ppm) undergoes a much slower degradation. This should be attributed to the instability of C═C double bond in propene. Apparent rate constants were roughly calculated by applying the pseudo-first-order reaction kinetics (Figure S4). As mentioned above, all three CeO_2 NCs present simple microstructures free of porous structure. In other words, when under light irradiation, the three samples probably own similar proportions of surface active area which can be illuminated by the incident photons. Taking the surface area differences into consideration, the normalized kinetic constants were summarized in Table 2. Notably, CeO_2 nanocubes (C−Cl) presented much better performance than nanorods, indicating the superiority of {100} facets in VOCs oxidation to {110} ones. On the other hand, compared to ceria nanorods, cube-like C−Cl showed a 4−5.7 times larger rate constant in propane degradation and a 1.9−3.2 times larger rate constant in propene degradation (Table 2). That is, ceria nanorods had achieved a comparative advantage for destruction of C═C double bonds, probably due to the presence of surface defects. Besides, R−NO was unexpectedly more reactive than R−Cl despite their identical morphologies and sizes, indicating the existence of other determinants in deciding the final photocatalytic performance.

Table 2. Normalized Reaction Kinetics Data of Multiple Photo-Oxidation Processes over CeO_2 NCs

items	C−Cl	R−Cl	R−NO
k_{C3H8}/S_{BET} (h^{-1} m^{-2} g)	0.04	0.007	0.01
k_{C3H6}/S_{BET} (h^{-1} m^{-2} g)	0.19	0.06	0.1
r_{O2}/S_{BET} (μmol h^{-1} m^{-2})	1.24	1.70	0.97
I_{OH}/S_{BET} (h^{-1} m^{-2} g)	1.35	0.52	0.63

Additional tests further verified the complexity in the photoreactivity orders of different CeO_2 samples. As indicated in Figure 2c, all three samples gave continuous oxygen production via photocatalytic water splitting. The slowing O_2 evolution is probably due to the photodeposition of Ag nanoparticles on ceria surface. On the basis of the average reaction rates after 6 h irradiation (Table 2), a photoreactivity order of R−Cl > C−Cl > R−NO can be obtained. Although no strict correspondence between the activities and surface areas is guaranteed in catalytic processes, one conclusion that can be drawn is that R−Cl is assuredly more reactive than cube-like C−Cl and rod-like R−NO.[33] Moreover, photocatalytic ·OH generation was studied on the basis of the fluorescence at 426 nm, stemming from the transient radicals capture (Figure 2d and S5). The normalized growth rates of the peak intensity of

DOI: 10.1021/acscatal.5b01128
ACS Catal. 2015, 5, 4851−4858

characteristic fluorescence (Table 2) obviously indicated that cube-like C−Cl was the most active, followed by the rod-like R−NO and R−Cl, successively. This reactivity order is quite similar to that in VOCs degradation. In summary, there exist variable priorities between different nanoshapes as well as between different samples of identical nanoshapes, dependent on the photocatalytic processes selected. Specific surface properties in addition to the general atomic and electronic structures decided by the exposed crystal facets are clearly suggested.

In order to decouple the above intricate photoreactivity orders, several surface factors (i.e., atomic, electronic, and defect structures) were integrally examined. Energy band structures of the three samples were studied by diffuse reflectance spectra (DRS) (Figure S6), electrochemical Mott−Schottky measurements (Figure S7), and valence band (VB) XPS spectra (Figure S8). As indicated in Figure 3a, CeO_2

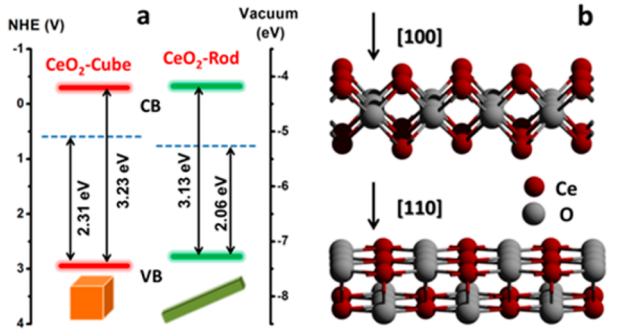

Figure 3. Energy band structures of different ceria nanoshapes (a). Slab models of atomic arrangement in different crystal facets (b).

nanocubes (C−Cl) own a larger band gap (3.23 eV) compared to the rod-like R−Cl and R−NO (3.13 eV). Besides, the VB of C−Cl lies more positively than that of the two rod-like samples. That is, once excited the photoinduced holes in C−Cl will exhibit superior oxidizing ability to those in R−Cl and R−NO. This difference in electronic structure should be the main reason for the heterogeneous activities in photo-oxidation that nanocubes behaved more energetically than nanorods. One exception in our tests is that R−Cl ({110} + {100}) was more efficient in oxygen evolution than {100}-dominated C−Cl. Given the higher surface energy of {100} facets (Figure 3b), there should be other competitive factors in addition to the surface electronic and atomic structures, probably related to surface defects.[24,26]

Different surface-defect distributions, which may have induced different photon-to-electron conversions, were initially speculated by the photoluminescence (PL) tests (Figure S9, Figure 4). As shown in Figure 4a, transient photocurrent curves were recorded over three ceria electrodes at a bias of 0.6 V (vs SCE). Obviously with regularly chopped light irradiation, three ceria samples present different photon-to-electron conversions. For further clarification, typical transient photocurrent responses via on−off cycles of light irradiation over three CeO_2 electrodes were collected in Figure 4b. Notably, the three samples present evident changes in the current transients when the light is on. For cube-like C−Cl, the initial anodic photocurrent spike and its subsequent decay is a typical indication of the surface recombination of photoinduced e^-/h^+ pairs.[37,38] However, for R−Cl, the anodic spike is much smaller after turning on the light. For R−NO, no anodic spike is

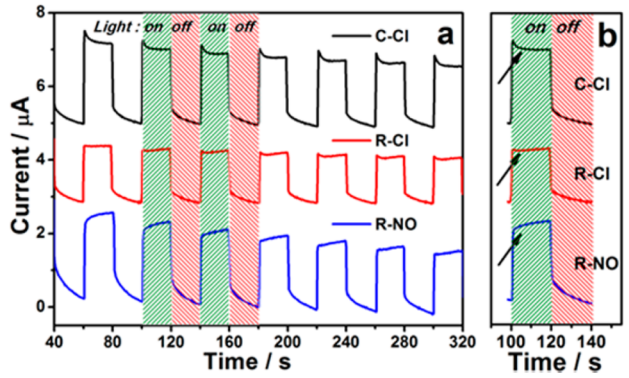

Figure 4. Transient current−time (i−t) curves of three ceria electrodes recorded under Xe lamp irradiation (a). The right panel (b) is one enlarged photocurrent transient for comparison.

observable, indicating that the recombination of photoinduced charge carriers has been greatly improved. It has been widely reported that surface heterojunctions constructed by various crystal facets with different valence band (VB) and conduction band (CB) positions can effectively improve the separation of photoinduced charge carriers within the semiconductor.[39,40] Therefore, the coexistence of {110} and {100} crystal facets within the rod-like samples may be one reason for the improved current transients of corresponding photoelectrodes (Figure 4).

However, as indicated in Figure 4b, the R−NO electrode obviously presents improved current transients compared to the R−Cl one, though the two samples own identical microscopic morphologies as well as crystallographic structures. That is, in addition to the surface heterojunction factor, there probably exist other influences on the charge separation process. Furthermore, the current amplitudes via light on−off cycles of R−NO electrode is obviously larger than that of the R−Cl one despite the similar surface areas of two CeO_2 NCs. This is another evidence of the promoted charge separation in R−NO, consistent with above discussion on the current spikes. The different behaviors of carriers separation should largely contribute to the different performance between the two rod-like samples in VOCs degradation and ·OH generation. Given the widely accepted positive roles of surface defects in charge separation, the above different photon-to-electron conversions are probably related to different surface structures of defects within the three samples.[12,41,42]

In order to explore the surface-defect structures of various CeO_2 NCs, several surface characterizations were employed. X-ray photoelectron spectroscopy (XPS) was used to identify the Ce^{3+} and O-vacancy sites on the surface. As shown in Figure 5a, the Ce $3d_{5/2}$ peaks of R−NO and R−Cl present successive shifts to lower binding energies compared to that of C−Cl, indicating increased e^--cloud density around the Ce nucleus.[43] It is thus suggested that there exist more Ce^{3+} ions on the surface of rod-like samples than nanocubes. This conjecture can be confirmed by the much enhanced intensity of Ce^{3+} peaks (u', u_0, v', and v_0) for R−NO and R−Cl when compared to C−Cl. On the other hand, as a result of the charge conservation, the presence of abundant Ce^{3+} ions on ceria surface proved by Ce 3d XPS (Figure 5a) probably induce surface oxygen vacancies, another important kind of defect sites in transition metal oxides.

As indicated in Figure 5b, the O 1s spectra of all three samples can be divided into three subpeaks, coming from the

DOI: 10.1021/acscatal.5b01128
ACS Catal. 2015, 5, 4851−4858

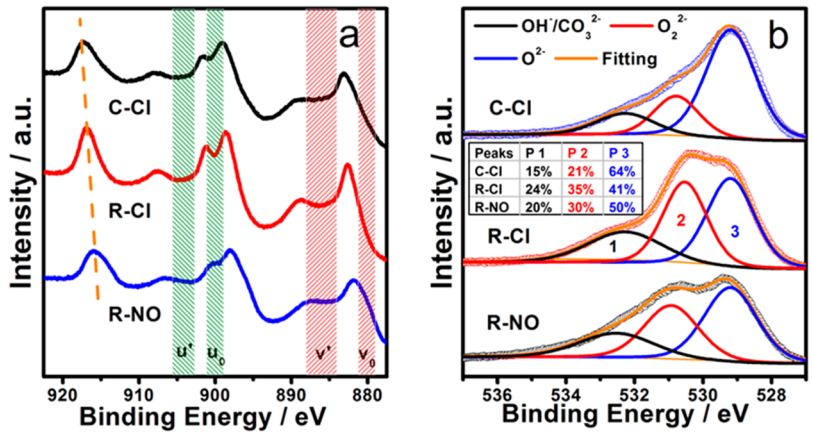

Figure 5. X-ray photoelectron spectroscopy (XPS) of C−Cl, R−Cl, and R−NO samples in Ce 3d (a) and O 1s (b) regions. Inset in the right panel (b) is the relative amount of various oxygen species.

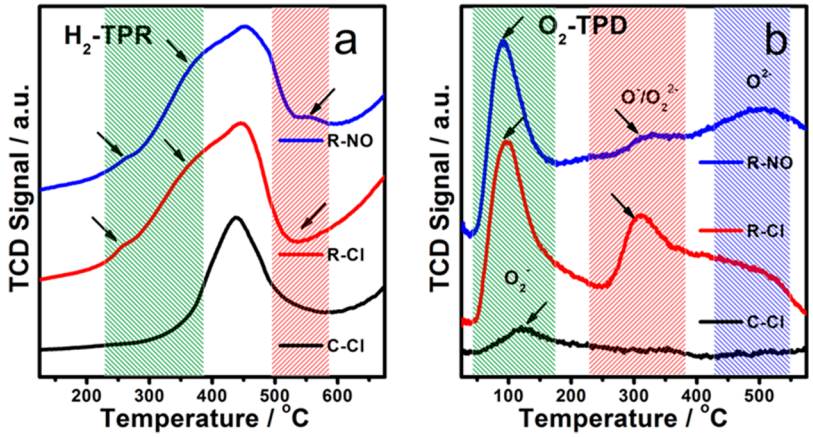

Figure 6. H_2-TPR (a) and O_2-TPD (b) profiles of three ceria samples.

coexisted surface O species, namely, surface hydroxyls, chemisorbed peroxy anions (O_2^{2-}), and lattice oxygen (O^{2-}).[20,43] Notably, C−Cl presents the highest ratio of lattice oxygen (64%) among the three samples. That is, ceria nanorods ({110} + {100}) have more O-vacancy defects than nanocubes ({100}), consistent with the theoretically predicted order of vacancies formation energy, {110} < {100}.[25,27] Taking the rule of charge conservation into consideration, this result is also in accordance with the discussions on Ce 3d XPS (Figure 5a), which show that there exist more Ce^{3+} ions on the surface of rod-like samples than nanocubes. Note that compared to C−Cl and R−NO, R−Cl owns a larger peak-area ratio of hydroxyls (24%), probably from the surface-bonded water molecules at defect sites. This may be one origin of the superior activity of R−Cl in photocatalytic oxygen evolution (Figure 2c), with efficient H_2O adsorption being the precondition of its subsequent splitting.

Recall that R−NO achieved much better performance than R−Cl in VOCs oxidation, though they have identical facet terminations as well as electronic structures. Temperature-programmed reduction in hydrogen (H_2-TPR) and desorption of oxygen (O_2-TPD) were conducted to further explore the surface differences among different samples (Figure 6). Notably in Figure 6a, R−NO and R−Cl present obvious H_2 consumption in the low-temperature zone (150−350 °C), which is negligible for C−Cl. This difference can be attributed to the abundant surface defects within ceria nanorods, as indicated by the XPS results. Moreover, R−NO shows the most prosperous TPR trace around medium temperatures (350−600 °C), indicating the superior reducibility of Ce atoms on its surface. Compared to R−Cl, the much enhanced reducibility of R−NO at medium and low temperatures (150−600 °C) should be one of the main reasons for its superior photoreactivity in VOCs oxidation.

On the other hand, oxygen including both lattice O and gaseous O_2 from the environment plays decisive roles in photocatalytic aerobic oxidations.[7] O_2-TPD helps get insights into the adsorbed O species, as well as the mobility of corresponding surface species.[7,20,29] As shown in Figure 6b, oxygen desorptions at about 100 and 330 °C are ascribed to the adsorbed superoxide (O_2^-) and peroxide (O^-) species, respectively. Notably, R−Cl and R−NO present greatly enhanced chemical O_2 adsorption compared to the cube-like C−Cl. This probably stems from the abundant vacancies on ceria nanorods, analogous to the case of TiO_2.[44] Compared to R−Cl, the more prosperous O_2 desorption between 50 to 350 °C of R−NO suggests that R−NO has achieved more efficient O_2 activation on its surface. Besides, compared to R−Cl, R−NO obviously shows a larger desorption peak above 450 °C, attributed to the release of lattice oxygen. This difference indicates that R−NO owns better surface mobility of lattice oxygen, consistent with its easier reduction in H_2 around 500 °C (Figure 6a).[7,29] Given the above discussions on the TPR and TPD tests, excellent surface mobility of lattice oxygen as

DOI: 10.1021/acscatal.5b01128
ACS Catal. 2015, 5, 4851−4858

well as efficient activation of gaseous O_2 within R−NO should be favorable for its superior performance in VOCs oxidation, compared to another rod-like R−Cl.

CONCLUSION

In summary, we elaborately studied the heterogeneous reactivity of CeO_2 nanocrystals with well-defined surface planes in multiple photocatalytic processes, including VOCs oxidation, O_2 evolution, and ·OH generation. Variable reactivity priorities were clearly found in various reactions between different nanoshapes as well as different samples of identical nanoshapes. Several surface factors were integrally examined to decouple the intricate reactivity orders, including surface facet terminations, electronic structures, and defect sites. A competition among the coexisted surface factors is suggested in deciding the final photoreactivity orders. As an instance in photocatalytic O_2 evolution, surface defects were evidently proved to render rod-like R−Cl with superior activity to cube-like C−Cl, which has more reactive {100} facets exposure and a more suitable VB position. The results provide further insights into the complex surface effects in semiconductor photocatalysis. It also underscores the significance of surface-defect structure as an essential supplement to the traditional CFE strategy for achieving desired solar energy utilization.

ASSOCIATED CONTENT

Supporting Information

The Supporting Information is available free of charge on the ACS Publications website at DOI: 10.1021/acscatal.5b01128.

XRD patterns, TEM images, and PL spectra of CeO_2 NCs. Transient FL spectra for hydroxyl radicals detection. Rate constant calculations of VOCs degradation. Evaluation of electronic structures for different CeO_2 nanoshapes (PDF)

AUTHOR INFORMATION

Corresponding Author

*E-mail: wzwang@mail.sic.ac.cn.

Notes

The authors declare no competing financial interest.

ACKNOWLEDGMENTS

We acknowledge the financial support from the National Basic Research Program of China (2013CB933200) and the National Natural Science Foundation of China (51272269, 51272303, and 51102262).

REFERENCES

(1) Yang, H. G.; Sun, C. H.; Qiao, S. Z.; Zou, J.; Liu, G.; Smith, S. C.; Cheng, H.-M.; Lu, G. Q. *Nature* **2008**, *453*, 638−641.
(2) Pan, J.; Liu, G.; Lu, G. Q. M.; Cheng, H.-M. *Angew. Chem., Int. Ed.* **2011**, *50*, 2133−2137.
(3) Liu, G.; Yang, H. G.; Pan, J.; Yang, Y. Q.; Lu, G. Q.; Cheng, H.-M. *Chem. Rev.* **2014**, *114*, 9559−9612.
(4) Li, R.; Zhang, F.; Wang, D.; Yang, J.; Li, M.; Zhu, J.; Zhou, X.; Han, H.; Li, C. *Nat. Commun.* **2013**, *4*, 1432.
(5) Long, J.; Chang, H.; Gu, Q.; Xu, J.; Fan, L.; Wang, S.; Zhou, Y.; Wei, W.; Huang, L.; Wang, X.; Liu, P.; Huang, W. *Energy Environ. Sci.* **2014**, *7*, 973−977.
(6) Yang, H. G.; Liu, G.; Qiao, S. Z.; Sun, C. H.; Jin, Y. G.; Smith, S. C.; Zou, J.; Cheng, H.-M.; Lu, G. Q. *J. Am. Chem. Soc.* **2009**, *131*, 4078−4083.
(7) Jiang, D.; Wang, W.; Sun, S.; Zhang, L.; Zheng, Y. *ACS Catal.* **2015**, *5*, 613−621.
(8) Ma, Y.; Wang, X.; Jia, Y.; Chen, X.; Han, H.; Li, C. *Chem. Rev.* **2014**, *114*, 9987−10043.
(9) Liu, G.; Yu, J. C.; Lu, G. Q. M.; Cheng, H.-M. *Chem. Commun.* **2011**, *47*, 6763−6765.
(10) Jiang, D.; Wang, W.; Gao, E.; Sun, S.; Zhang, L. *Chem. Commun.* **2014**, *50*, 2005−2007.
(11) Chen, Z. G.; Wang, Q.; Wang, H. L.; Zhang, L. S.; Song, G. S.; Song, L. L.; Hu, J. Q.; Wang, H. Z.; Liu, J. S.; Zhu, M. F.; Zhao, D. Y. *Adv. Mater.* **2013**, *25*, 2095−2100.
(12) Guan, M.; Xiao, C.; Zhang, J.; Fan, S.; An, R.; Cheng, Q.; Xie, J.; Zhou, M.; Ye, B.; Xie, Y. *J. Am. Chem. Soc.* **2013**, *135*, 10411−10417.
(13) Fu, Q.; Saltsburg, H.; Flytzani-Stephanopoulos, M. *Science* **2003**, *301*, 935−938.
(14) Liu, X. W.; Zhou, K. B.; Wang, L.; Wang, B. Y.; Li, Y. D. *J. Am. Chem. Soc.* **2009**, *131*, 3140−3141.
(15) Si, R.; Flytzani-Stephanopoulos, M. *Angew. Chem.* **2008**, *120*, 2926−2929.
(16) Sun, C.; Li, H.; Chen, L. *Energy Environ. Sci.* **2012**, *5*, 8475−8505.
(17) Tanaka, A.; Hashimoto, K.; Kominami, H. *J. Am. Chem. Soc.* **2012**, *134*, 14526−14533.
(18) Primo, A.; Marino, T.; Corma, A.; Molinari, R.; Garcia, H. *J. Am. Chem. Soc.* **2011**, *133*, 6930−6933.
(19) Jiang, D.; Wang, W.; Gao, E.; Zhang, L.; Sun, S. *J. Phys. Chem. C* **2013**, *117*, 24242−24249.
(20) Jiang, D.; Wang, W.; Zhang, L.; Qiu, R.; Sun, S.; Zheng, Y. *Appl. Catal., B* **2015**, *165*, 399−407.
(21) Aneggi, E.; Wiater, D.; de Leitenburg, C.; Llorca, J.; Trovarelli, A. *ACS Catal.* **2014**, *4*, 172−181.
(22) Mai, H.-X.; Sun, L.-D.; Zhang, Y.-W.; Si, R.; Feng, W.; Zhang, H.-P.; Liu, H.-C.; Yan, C.-H. *J. Phys. Chem. B* **2005**, *109*, 24380−24385.
(23) Zhang, J.; Kumagai, H.; Yamamura, K.; Ohara, S.; Takami, S.; Morikawa, A.; Shinjoh, H.; Kaneko, K.; Adschiri, T.; Suda, A. *Nano Lett.* **2011**, *11*, 361−364.
(24) Conesa, J. *Surf. Sci.* **1995**, *339*, 337−352.
(25) Nolan, M.; Fearon, J. E.; Watson, G. W. *Solid State Ionics* **2006**, *177*, 3069−3074.
(26) Nolan, M.; Grigoleit, S.; Sayle, D. C.; Parker, S. C.; Watson, G. W. *Surf. Sci.* **2005**, *576*, 217−229.
(27) Nolan, M.; Parker, S. C.; Watson, G. W. *Surf. Sci.* **2005**, *595*, 223−232.
(28) Sayle, D. C.; Maicaneanu, S. A.; Watson, G. W. *J. Am. Chem. Soc.* **2002**, *124*, 11429−11439.
(29) Wu, Z.; Li, M.; Howe, J.; Meyer, H. M.; Overbury, S. H. *Langmuir* **2010**, *26*, 16595−16606.
(30) Wu, Z.; Li, M.; Overbury, S. H. *J. Catal.* **2012**, *285*, 61−73.
(31) Mann, A. K. P.; Wu, Z.; Calaza, F. C.; Overbury, S. H. *ACS Catal.* **2014**, *4*, 2437−2448.
(32) Wu, Z.; Schwartz, V.; Li, M.; Rondinone, A. J.; Overbury, S. H. *J. Phys. Chem. Lett.* **2012**, *3*, 1517−1522.
(33) Yao, S. Y.; Xu, W. Q.; Johnston-Peck, A. C.; Zhao, F. Z.; Liu, Z. Y.; Luo, S.; Senanayake, S. D.; Martinez-Arias, A.; Liu, W. J.; Rodriguez, J. A. *Phys. Chem. Chem. Phys.* **2014**, *16*, 17183−17195.
(34) Zhao, F.; Liu, Z.; Xu, W.; Yao, S.; Si, R.; Johnston-Peck, A.; Martínez-Arias, A.; Hanson, J.; Senanayake, S.; Rodriguez, J. *Catal. Lett.* **2015**, *145*, 808−815.
(35) Braslavsky, S. E.; Braun, A. M.; Cassano, A. E.; Emeline, A. V.; Litter, M. I.; Palmisano, L.; Parmon, V. N.; Serpone, N. *Pure Appl. Chem.* **2011**, *83*, 931−1014.
(36) Gao, E.; Wang, W. *Nanoscale* **2013**, *5*, 11248−11256.
(37) Hebda, M.; Stochel, G.; Szaciłowski, K.; Macyk, W. *J. Phys. Chem. B* **2006**, *110*, 15275−15283.
(38) Long, M.; Cai, W.; Kisch, H. *J. Phys. Chem. C* **2008**, *112*, 548−554.

DOI: 10.1021/acscatal.5b01128
ACS Catal. 2015, 5, 4851−4858

(39) D'Arienzo, M.; Dozzi, M. V.; Redaelli, M.; Credico, B. D.; Morazzoni, F.; Scotti, R.; Polizzi, S. *J. Phys. Chem. C* **2015**, *119*, 12385−12393.
(40) Yu, J.; Low, J.; Xiao, W.; Zhou, P.; Jaroniec, M. *J. Am. Chem. Soc.* **2014**, *136*, 8839−8842.
(41) Bi, W.; Ye, C.; Xiao, C.; Tong, W.; Zhang, X.; Shao, W.; Xie, Y. *Small* **2014**, *10*, 2820−2825.
(42) Zhu, Q.; Peng, Y.; Lin, L.; Fan, C.-M.; Gao, G.-Q.; Wang, R.-X.; Xu, A.-W. *J. Mater. Chem. A* **2014**, *2*, 4429−4437.
(43) Ferreira, V. c. J.; Tavares, P.; Figueiredo, J. L.; Faria, J. L. *Ind. Eng. Chem. Res.* **2012**, *51*, 10535−10541.
(44) Setvín, M.; Aschauer, U.; Scheiber, P.; Li, Y.-F.; Hou, W.; Schmid, M.; Selloni, A.; Diebold, U. *Science* **2013**, *341*, 988−991.

DOI: 10.1021/acscatal.5b01128
ACS Catal. 2015, 5, 4851−4858